



Photodegradation of DMMP and CEES on zirconium doped titania nanoparticles

Andreas Mattsson^a, Christian Lejon^a, Václav Štengl^b, Snejana Bakardjieva^b,
František Opluštil^c, Per Ola Andersson^a, Lars Österlund^{a,d,*}

^a FOI, SE-901 82 Umeå, Sweden

^b Institute of Inorganic Chemistry AS CR v.v.i., 250 68 Řež, Czech Republic

^c Military Technical Institute of Protection Brno, Veseláská 230, 628 00 Brno, Czech Republic

^d Department of Solid State Physics, The Ångström Laboratory, Uppsala University, SE-751 21 Uppsala, Sweden

ARTICLE INFO

Article history:

Received 16 June 2009

Received in revised form 11 August 2009

Accepted 22 August 2009

Available online 28 August 2009

Keywords:

TiO₂
Zirconium
Photocatalysis
DMMP
CEES
FTIR
Raman

ABSTRACT

The structure and photocatalytic activity of Zr doped TiO₂ nanocrystallites with a varying Zr content between 0 and 15 wt% prepared by an efficient and environmentally benign method has been studied by vibrational spectroscopy, TEM and XRD. It is shown that the presence of Zr⁴⁺ ions stabilizes the anatase structure and delays phase transformation to rutile upon annealing as well as retarding grain coarsening. All TiO₂ samples up to 13 wt% Zr doping concentration show better or similar photoreactivity compared to P25 (Degussa) for decomposition of adsorbed 2-chloroethyl ethyl sulphide (CEES) and dimethyl methylphosphonate (DMMP) in synthetic air at room temperature. The most efficient sample for photodegradation of both CEES and DMMP is shown to be titania doped with 6.8 wt% Zr. The photodegradation of CEES is faster than DMMP under the same experimental conditions. On the undoped TiO₂ sample urea residues are detected spectroscopically. Much less is detected on the Zr doped samples. Mode resolved in situ FTIR surface spectroscopy enables distinction of CEES or DMMP, decomposition products as well as the influence of residues from the particle synthesis. This facilitates extraction of intra-comparable reaction rates. Possible explanations for the improved reactivity of the Zr doped titania are discussed.

© 2009 Elsevier B.V. All rights reserved.

1. Introduction

Large efforts are currently devoted to development of new photoactive semiconductors that are able to convert light (and ultimately sunlight) into useful chemical or electrical energy. Wide band gap metal oxides belong to these classes of materials with TiO₂ being by far the most studied photocatalytic material [1]. These photocatalytic materials are interesting for pollutant degradation in new environmental clean-up technologies, where photoinduced surface reactions oxidatively decomposes harmful pollutants and convert them into harmless products, and ultimately only CO₂, H₂O and mineral acids [2,3]. A major challenge is to develop photocatalytic materials that on one hand are effective (high quantum yield, durable, i.e. stable over long periods of usage, and capable of broad spectrum pollutant degradation), and on the other hand are cheap to manufacture in large quantities and readily implemented in the intended application (most often added as an “outer” coating on a supporting material) [4]. Here we report on photoinduced

degradation of two simle chemical warfare agents (CWA) for sarin (dimethyl methylphosphonate, DMMP) and mustard (2-chloroethyl ethyl sulphide, CEES), respectively, on Zr doped anatase TiO₂ nanoparticles prepared by a simple and cost-effective methods and evaluate their properties as potential photocatalytic materials for CWA and pesticide decontamination.

Zirconium doped TiO₂ (Zr:TiO₂) has previously been reported to yield enhanced photocatalytic activity for 2-chlorophenol decomposition [5]. Several preparation methods are today known to produce Zr:TiO₂ materials including inverse microemulsion [6] and sol–gel method [5,7] as well as a few others (see references in Lukáč et al. [8]). In the present study a more cost-effective and environmentally benign method is used where homogenous precipitation of acid aqueous solutions of TiOSO₄ with urea is applied to obtain Zr:TiO₂ nanocrystallites with a varying Zr content between 0 and 15 wt%. We described the synthetic procedure in detail in previous publications [8,9]. To gain further insights in the fundamental properties of these materials for model pesticide and CWA photocatalytic degradation we here report vibration spectroscopy data revealing detailed information on structure and stability of the catalysts as well as molecular transformations occurring on the nanoparticles upon photon irradiation. The synthesized Zr:TiO₂ are characterized with respect to crystallite size, specific surface area, morphology and phase stability, and the

* Corresponding author at: FOI, Cementv. 20, SE-901 82 Umeå, Sweden.
Tel.: +46 90 106900; fax: +46 90 106800.

E-mail address: lars.osterlund@foi.se (L. Österlund).

photocatalytic capacity of the material is studied by in situ diffuse reflectance Fourier transform infrared spectroscopy (DRIFTS) experiments from which photodegradation rates are determined.

2. Experimental

2.1. Preparation of zirconium doped titania samples

The sample preparation method was adopted from Lukáč et al. [8] and has been described in detail therein. Briefly, Zr^{4+} doped nanocrystalline titania was obtained from homogenous hydrolysis of $TiOSO_4$ and $ZrOSO_4$ aqueous solutions using urea as precipitation agent. The formed precipitates were washed by distilled water with decantation, filtered off and dried. By this method five samples were prepared denoted as TiZr1–TiZr5, containing varying amount of Zr (Table 1). An undoped sample was also synthesized denoted TiZr0.

2.2. Characterization methods

Physical characterization of similar $Zr:TiO_2$ nanoparticles have earlier been described by Štengl et al. [9]. Here we report on complementary XRD and TEM data as well as a detailed vibrational spectroscopy characterization (Raman and DRIFT spectroscopy).

X-ray diffraction (XRD) patterns were obtained by a Siemens D5005 instrument using $Cu\ K\alpha$ radiation (40 kV, 30 mA) and a diffracted beam monochromator. Data were collected from 5° to 90° in a step-scan mode. Qualitative phase analysis was performed with EVA Application and Xpert HighScore utilizing JCPDS PDF-2 database [10].

Rietveld refinement of the XRD spectra and size determination was performed with the Bruker TOPAS software. This analysis yielded a slightly different crystal size than previously reported values [9].

Transmission electron microscopy (TEM) was performed with a Philips EM 201 operating at 80 kV. High-resolution TEM (HRTEM) imaging was carried out by using a JEOL JEM 3010 operating at 300 kV (LaB_6 cathode) that gives a point resolution of 1.7 Å. A copper grid coated with a porous carbon support film was applied for TEM sample preparation. The powder was dispersed in ethanol and the suspension was treated in ultrasound for 10 min. Scanning electron microscopy (SEM) studies were performed using a Philips XL30 CP microscope equipped with energy dispersive X-ray (EDX), Robinson, secondary electron (SE) and back-scattered electron (BSE) detectors.

Raman spectroscopy was carried out in backscattering geometry using a Horiba Jobin-Yvon Labram HR800 confocal Raman microscope. A diode laser beam employing $\lambda = 785\text{ nm}$ with output power of 30 mW was focused on the sample by a $50\times$ long working objective (Nikon, NA = 0.45 and WD = 17 mm). The spectral

resolution was ca. 3.5 cm^{-1} employing a 600 grooves/mm grating. The spectra were frequency calibrated against the intense Raman active mode of silicon at 520.7 cm^{-1} . For detailed analysis of the low frequency anatase E_g mode a 1800 grooves/mm grating was used yielding a spectral resolution of $\sim 1\text{ cm}^{-1}$. No local heating effects from the Raman laser source were observed as compared to using lower intensities. Experiments were made to check the influence of sample preparation impurities. Although the Raman results did not reveal any qualitative effect of different sample pre-treatments, the results presented here were all calcined at 673 K for 24 h and subsequently washed in 1 mM NaOH as previously described [12] before Raman experiments. The $Zr:TiO_2$ samples were successively annealed in a temperature cell (Linkam TS 1500) at elevated temperatures for 2 h, and then cooled to 298 prior to Raman measurements. Anneals started at 873 K and were repeated with the same sample in steps of increasing 100 K until the completion of the anatase to rutile phase transition. Because of a temperature gradient between the thermocouple and the position where Raman spectra were acquired the reported temperatures are overestimated by up to 150 K for anneals at higher temperatures and less for lower annealing temperatures.

Raman scattering is more sensitive than XRD to detect and distinguish small amounts of a foreign crystalline phase in mixed phase solids [13]. Here we have used Raman spectroscopy to follow the anatase to rutile transition by comparing the area of rutile absorption bands at ~ 447 and $\sim 612\text{ cm}^{-1}$ to anatase peaks at ~ 399 , ~ 516 , and $\sim 640\text{ cm}^{-1}$ (cf. Table 2). The rutile content in the samples was estimated by the following expression:

$$\alpha = \frac{\sum_{j=447,612} \sigma_{R,j}}{\sum_{j=447,612} \sigma_{R,j} + \sum_{j=399,516,640} \sigma_{A,j}} \times 3.47 \quad (1)$$

where σ_{ij} is the peak area of a peak at wavenumber j from the crystalline phase i . The scale factor 3.47 is a modification of the calibration curve reported by Bassi et al. [14]. It is constructed to exclude the strong E_g vibration at 144 m^{-1} , which was used in reference [14], since our instrumental set-up did not allow us to acquire the complete low-wavenumber tail of the anatase E_g vibration.

2.3. Photocatalytic experiments

Diffuse reflectance infrared Fourier transform spectroscopy (DRIFTS) was performed with a vacuum pumped FT-IR spectrometer (Bruker IFS 66v/S) equipped with a modified DRIFT Praying Mantis reaction cell (Harrick) that allowed for in situ adsorption and reaction experiments with simultaneous illumination and QMS or GC–MS gas phase analysis of reaction products [15,16]. Repeated DRIFT spectra were acquired as a function of time by collecting 68 scans (30 s) followed by a 30-s long dwell time

Table 1

Material properties for the different samples as well as rate constants, k , obtained during the first 15 min of illumination and the time it takes to remove CEES and DMMP until 10% of the initial peak area is left, t_{10} . For the rate constants and removal time values are given for the integrated absorbance bands in the C–H region whereas values inside parenthesis are for a mode specific band. Zr concentration and BET area is obtained from Ref. [9].

Sample name	Crystal structure	EDX Zr conc. (wt%)	XRD anatase crystallite size (nm)	BET ($\text{m}^2\text{ g}^{-1}$)	DMMP		CEES	
					k (min^{-1})	t_{10} (min)	k (min^{-1})	t_{10} (min)
TiZr0	Anatase	0	6.9	200	0.05 (0.11)	>115 (21)	0.14 (0.15)	18 (12)
TiZr1	Anatase	1.5	9.2	163	0.07 (0.11)	63 (24)	0.12 (0.15)	22 (12)
TiZr2	Anatase	6.8	10.0	167	0.07 (0.11)	55 (24)	0.13 (0.16)	23 (14)
TiZr3	Anatase	8.8	10.7	210	0.05 (0.09)	>115 (38)	0.10 (0.13)	–(18) ^a
TiZr4	Anatase	13.2	13.4	282	0.05 (0.08)	114 (55)	0.07 (0.11)	64 (27)
TiZr5	Amorphous	15.2	–	27	0.01 (0.01)	>115 (>115)	0.01 (0.02)	>115 (>115)
P25	Anatase/rutile mix				0.06 (0.09)	83 (39)	0.07 (0.08)	62 (44)

^a After ca. 15 min there is a kink in the curve and no further decrease of the absorbance band indicating that the signal disappears in the background noise.

Table 2

Raman shifts (cm^{-1}) and peak assignments of the Zr doped samples used in this study; reported are peak positions after calcination in the anatase modification and the peak positions of rutile modification which was present after annealing of TiO_2 [21,29]. The differences in peak positions between samples and literature are effects of doping and phonon confinement further discussed in the text. n/a means not available.

Sample	Anatase				Rutile			
	E_g	$B_{1g} + A_{1g}$	B_{1g}	E_g	A_{1g}	E_g	Comb.	B_{1g}
TiZr0	644	517	398	149	611	446	240	n/a
TiZr1	641	516	397	148	612	446	236	143
TiZr2	642	517	397	148	612	446	234	n/a
TiZr3	639	516	395	148	613	443	231	141
TiZr4	639	516	395	146	613	437	238	141
TiZr5	Amorphous	Amorphous	Amorphous	Amorphous	613	439	238	142
Ref. [21,29]	639	513–519	399	144	612	447	~235	143

between consecutive measurements. Post-treatments of spectra included smoothing with Savitzky-Golay method using a 9-data point window and base line corrections. Prior to each measurement samples were annealed at 673 K in a flow of 100 ml min^{-1} of synthetic air (80% N_2 , 99.994% purity and 20% O_2 , 99.999% purity) for 15 min and cooled to 20°C in the same gas. Organic contaminants from normal storage in ambient conditions are normally readily removed by this procedure, as we have repeatedly proved on a wide selection of TiO_2 powder samples prepared by sol-gel and microemulsion methods [17–19]. The sample prepared in this manner can be considered oxidized and hydroxylated with preadsorbed OH groups (from background gas), as well as O_2 and O adatoms. However, as we have previously demonstrated in detail this procedure is not sufficient to remove all urea residues in the undoped TiO_2 sample (TiZr0) and requires an extended pre-treatment procedure [12]. Fortunately, the Zr doped samples (TiZr1–TiZr5) appeared spectroscopically clean without any further pre-treatments. In the present study the focus has been to scrutinize as-prepared samples (Section 2.1) without elaborate pre-treatments which are arguably technologically most relevant. Therefore in order to facilitate comparable analysis on samples representative we have chosen not to perform further pre-treatments of any of the samples TiZr0–TiZr5.

Liquid 2-chloroethyl ethyl sulphide (CEES; 98% GC purity, Sigma–Aldrich) and dimethyl methylphosphonate (DMMP, 97% GC purity, Sigma–Aldrich) where used as delivered and introduced into the gas feed via a gas generator as described elsewhere [19]. Briefly the liquids were heated to 335 K and evaporated into a gas stream of synthetic air through a diffusion tube. The calibrated dose rate was ≈ 17 and $\approx 6.5 \mu\text{g min}^{-1}$ for CEES and DMMP, respectively. Evaporation was typically performed for 15 min (CEES) or 25 min (DMMP) followed by flushing of the reaction cell with synthetic air for 15 min prior to UV illumination.

Photon irradiation was done with a 300-W Xe lamp coupled to an optical fibre bundle to illuminate the sample through a CaF_2 window. The light was directed through a 75-mm long water filter to remove the infrared part of the spectrum. The measured photon power was 290 mW cm^{-2} in the wavelength region $200 < \lambda < 800 \text{ nm}$, and 30 mW cm^{-2} for $\lambda < 390 \text{ nm}$ (corresponding to the optical band gap of anatase TiO_2).

3. Results and discussion

3.1. Materials structure and morphology

The XRD patterns and characteristic 2θ values of the diffraction peaks for the pure and the Zr^{4+} doped titania correspond to anatase structure (ICDD PDF 21-1272) [10], which also is confirmed by the Raman spectroscopic measurements discussed below. With increasing Zr concentration up to sample TiZr4, which contains 13.2 wt% Zr, the particle diameter increase from ca. 7 to 13 nm (Table 1). The diffraction pattern of samples TiZr5 is characteristic

for amorphous materials, in agreement with the Raman data discussed below. The collapse of the anatase crystal structure at high Zr content has earlier been ascribed to $[\text{Zr}(\text{OH})_n]^{4-n}$ complexes, which prevent formation of crystalline particles and thus lead to gel precipitation [20].

From SEM micrographs shown in Fig. 1 it is evident that the synthesized powders, TiZr0–5, form spherically shaped aggregates of rather narrow size distribution of 1–2 μm in diameter. An EDX analysis of the particles is presented in Table 1. Based on the HRTEM results (Fig. 2) it is seen that the spherical aggregates consist of primary 8–10 nm anatase nanocrystals interlaid by a small fraction of amorphous material. In particular the HRTEM micrographs in Fig. 2a–d show the surface morphology of the sample TiZr4 containing 13.2 wt% Zr and show nanosized titania with well-developed crystallinity. The interlayer spacing of $d = 0.35 \text{ nm}$ corresponds to the (101) planes in anatase (Fig. 2b). As previously reported image processing analysis of the HRTEM micrographs and SAED analysis were done to extract the refined microstructures and explore grain boundaries and confirm the anatase structure determined from XRD [9].

The measured BET surface area of the Zr: TiO_2 powders was determined to be between 160 and $280 \text{ m}^2 \text{ g}^{-1}$ with the sample TiZr4 exhibiting the largest area (Table 1) [9]. The low surface area for sample TiZr5 is due to the amorphous TiO_2 forming highly dense aggregates with little porosity (the pore volume for sample TiZr5 is almost a factor of 10 lower compared to the other samples [9]). In Ref. [9] it was shown that an even higher Zr dopant concentration yielded amorphous ZrO_2 that exhibited higher surface area than corresponding amorphous TiO_2 present in sample TiZr5.

3.2. Raman spectroscopy

Raman spectroscopy is an established technique to study crystal structures. Raman spectra of anatase and rutile crystal phases differ significantly and can be used to study phase transitions in TiO_2 [21]. Raman spectra of the samples containing up to 13% Zr (TiZr0–TiZr4) calcined 24 h at 673 K all show that Zr: TiO_2 is present in the anatase modification. The specific vibration modes are located around 144 cm^{-1} (E_g), 397 cm^{-1} (B_{1g}), 517 cm^{-1} ($B_{1g} + A_{1g}$) and 640 cm^{-1} (E_g) (Table 2 and Fig. 3a). The measured frequencies of peak positions vary between the samples. For example the low frequency E_g mode progressively downshifts from 149.2 to 145.5 cm^{-1} with increased doping concentration (Table 2). At 15% Zr (TiZr5) the particles are present in an amorphous phase displaying a spectrum with a broad background with no clear bands and represents the phonon density of state (Fig. 3a) [22].

Raman spectra of the as prepared samples up to 13% Zr (TiZr0–TiZr4) show that TiO_2 is present in the anatase modification in agreement with the XRD results. At 15% Zr (TiZr5) the synthesis results in amorphous particles. In addition to the well-known

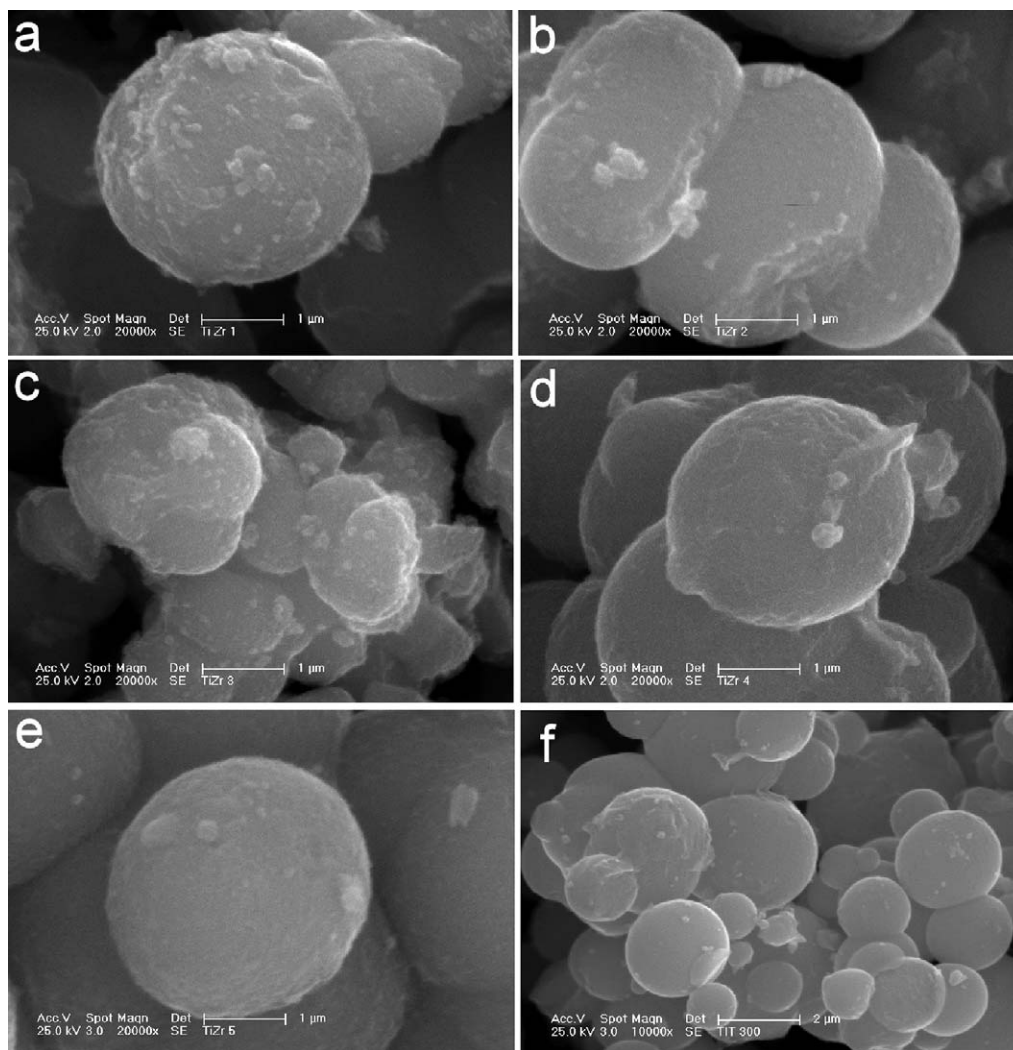


Fig. 1. SEM images of (a) TiZr1, (b) TiZr2, (c) TiZr3, (d) TiZr4, (e) TiZr5 and (f) undoped TiO₂.

peaks of TiO₂ anatase structure a weak peak at 250 cm^{-1} is seen for the samples TiZr1–TiZr3 (as-prepared). This band does not correspond to any symmetry allowed modes in ZrO₂ [11]. This peak has earlier been observed in lanthanoid doped TiO₂ [23], but its origin is still unknown. At present we therefore can only infer that it is related to Zr doping. The position of the Eg mode shifts to lower frequency as a function of calcination and annealing temperature. Simultaneously the width of the peak decreases. However, for samples containing more than 9% Zr (TiZr4 and TiZr5), the peak position shifts in opposite direction towards higher wavenumbers and abruptly narrows at annealing temperatures of 1373 K and higher. This is likely due to phase separation and precipitation of TiZrO₄ and ZrO₂ [24–26]. The narrowing and frequency downshift as function of annealing can be explained by the well-known phonon confinement effect [22]. It is known that phonons confined into the nanometer size regime exhibits a broadened Raman line profile as well as a shift in peak position due to the breakdown of the $\Delta q = 0$ momentum selection rule for the photon–phonon interaction. The anatase low frequency Eg mode shifts to higher frequency and asymmetrically broadens as an effect of phonon confinement in a nanocrystal [27]. The decrease of both width and peak position with annealing temperature (samples TiZr0–TiZr3 and TiZr4 and TiZr5 up to 1273 K) is thus attributed to grain growth. At lower temperatures,

typically employed in our calcination pre-treatments (673 K), the decrease rather originate from transformation of small amorphous content to the already existing nanocrystals.

Phase transition from anatase to rutile occurs for all samples upon annealing and the relative amounts of the anatase and rutile content estimated by Eq. (1) is visualized in Fig. 3b. Clearly, the phase transition temperature is delayed by the incorporation of Zr into the anatase lattice, which agrees with the findings in related works [26,28]. In Fig. 3c a sequence of Raman spectra of TiZr5 is shown which demonstrates the crystallization of the amorphous phase into anatase and further transformation to rutile as function of annealing temperature. There is no evidence of any other phase than anatase in the Raman spectrum of TiZr5 annealed for 2 h at 873 K in air. The rutile phase is easily identified by peaks at $\sim 235\text{ cm}^{-1}$ (combination band), 447 cm^{-1} (E_g) and $612\text{ (A}_{1g})\text{ cm}^{-1}$ [29] with the exact wavenumbers depending on Zr concentration (Table 2). The variation of peak position between samples in the rutile modification is entirely an effect of doping and not an effect of phonon confinement due to their larger grain sizes. Zhang et al. report $\sim 14\text{ nm}$ as a critical size of TiO₂ nanoparticles for the anatase to rutile transition. This is larger than the upper limit of $\sim 10\text{ nm}$ required for the phonon confinement effect to be significant in rutile crystals [30,31].

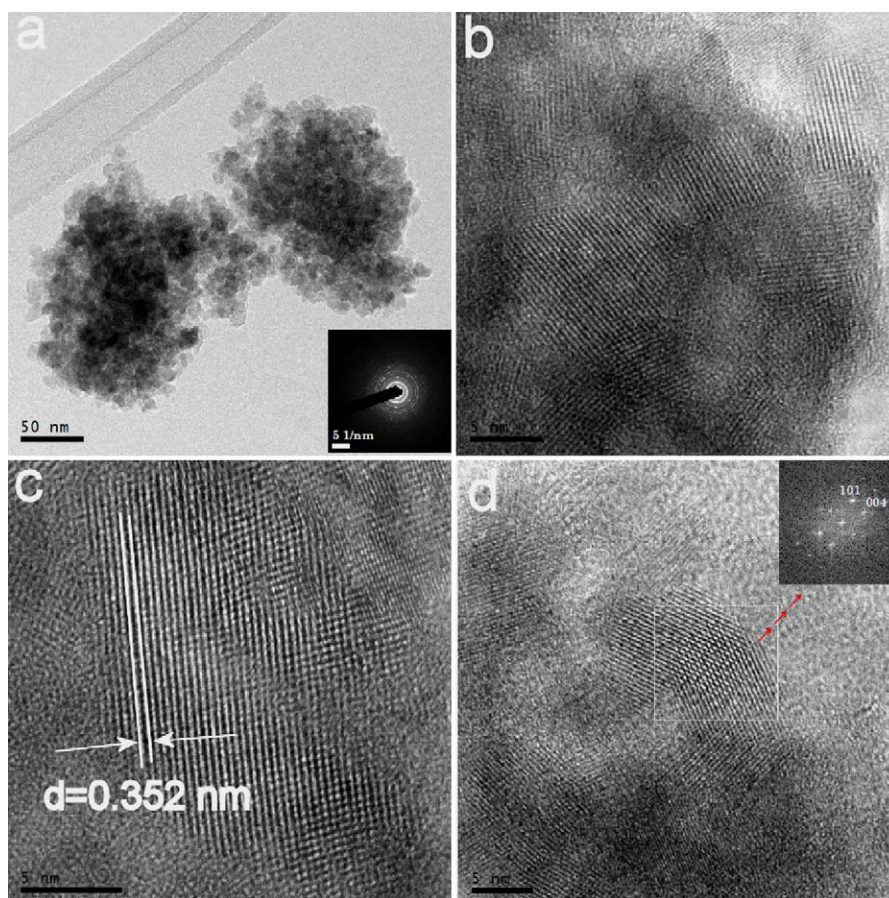


Fig. 2. High-resolution TEM micrographs of Zr^{4+} doped titania (sample TiZr4): (a) magnification 80,000; (b)–(d) show images that are enlarged parts of the image shown in (a).

4. Adsorption and photodegradation of DMMP and CEES on $\text{Zr}:\text{TiO}_2$

4.1. DMMP adsorption

Fig. 4 shows DRIFT spectra of DMMP adsorbed on TiZr0, TiZr2 and TiZr4. Corresponding measurements performed on a reference TiO_2 powder sample (P25 from Degussa) were also made. The DRIFT spectra of DMMP adsorbed on $\text{Zr}:\text{TiO}_2$ appear qualitatively similar for all samples in the TiZr series (Fig. 4). The most pronounced absorption bands are due to the $\nu(\text{P}-\text{CH}_3)$ at 1186 cm^{-1} , $\nu(\text{P}=\text{O})$ at $\sim 1215\text{ cm}^{-1}$, and the symmetric $\delta(\text{CH}_3\text{P})$ stretching mode at 1315 cm^{-1} . Additionally, the symmetric and asymmetric $\nu(\text{C}-\text{O})$ peaks located at ca. 1042 and 1061 cm^{-1} , respectively, can be seen on all samples [15,32–34]. The measured vibrational frequencies are lower compared to those for liquid DMMP and is in good agreement with previous results where a downshift of the peak position is found upon metal coordination [15,34,35] and indicates that the DMMP is bonded to the surface with the $\text{P}=\text{O}$ group. Absorbance peaks associated with Ti-coordinated methoxy groups are also seen in the fingerprint region ($\nu_{\text{as}}(\text{C}-\text{O})$ mode at 1118 cm^{-1}) and more clearly in the $\nu(\text{CH})$ region ($\nu_{\text{s}}(\text{CH}_3\text{O})$ mode at 2829 cm^{-1}) [34]. This incomplete dissociative pathway suggests that methoxy groups are formed by thermal dissociation of some DMMP molecules. In the hydroxyl $\nu(\text{OH})$ region negative absorbance bands due to disappearance of isolated Ti-OH groups are seen, while the increase of the broad peaks between ca. 3450 and 3600 and 3200 – 3400 cm^{-1} show that loosely bonded hydroxyls and water, respectively, are formed on the surface of the catalyst. This is also seen in the broad bulk water $\delta(\text{HOH})$ band at ca. 1650 cm^{-1} where a shoulder discernable at ca.

1630 cm^{-1} shows presence of adsorbed water. At 3773 cm^{-1} an absorbance band, which increases in intensity with increasing Zr content in the samples is seen. This absorption band is attributed to Zr-OH species based on previous reports of higher surface acidity of surface Zr-OH groups compared to Ti-OH [6,36].

4.2. CEES adsorption

In Fig. 5 is shown spectra of CEES adsorbed on TiZr0, TiZr2 and TiZr4. Corresponding measurements performed on a reference TiO_2 powder sample (P25) were also made. Typical adsorption peaks corresponding to CEES are seen on all samples, albeit with a few differences [37,38]. The $\delta(\text{CH}_2\text{S})$ mode at 1221 cm^{-1} is only seen on the pure TiO_2 sample and only as a small shoulder. The peak at 1185 cm^{-1} on TiZr0 is shifted to ca. 1175 cm^{-1} on the samples with Zr. This peak is not seen in liquid CEES [38] and may be attributed to C-O moieties which exhibit stretching frequencies in this region [37,39], viz. $\text{Ti}-\text{O}-\text{CH}_2-$ species due to dechlorinated CEES or formation of ethoxy species by reactions with oxygen. In the $\nu(\text{C}-\text{H})$ stretching region the most pronounced CEES peaks are found at approximately the same wavenumbers for all samples. The exact assignment of these peaks is nonetheless a bit ambiguous due to overlapping bands of the CH_x groups in the CEES molecule [37,40]. Again displacement of surface hydroxyls, water formation and a band at 3773 cm^{-1} due to Zr-OH is identified in the DRIFT spectra.

4.3. Photodegradation of DMMP

Upon band gap irradiation all DMMP peaks decrease with irradiation time (Fig. 6). This shows that the functional groups in the DMMP molecule dissociate. Appearance of new broad

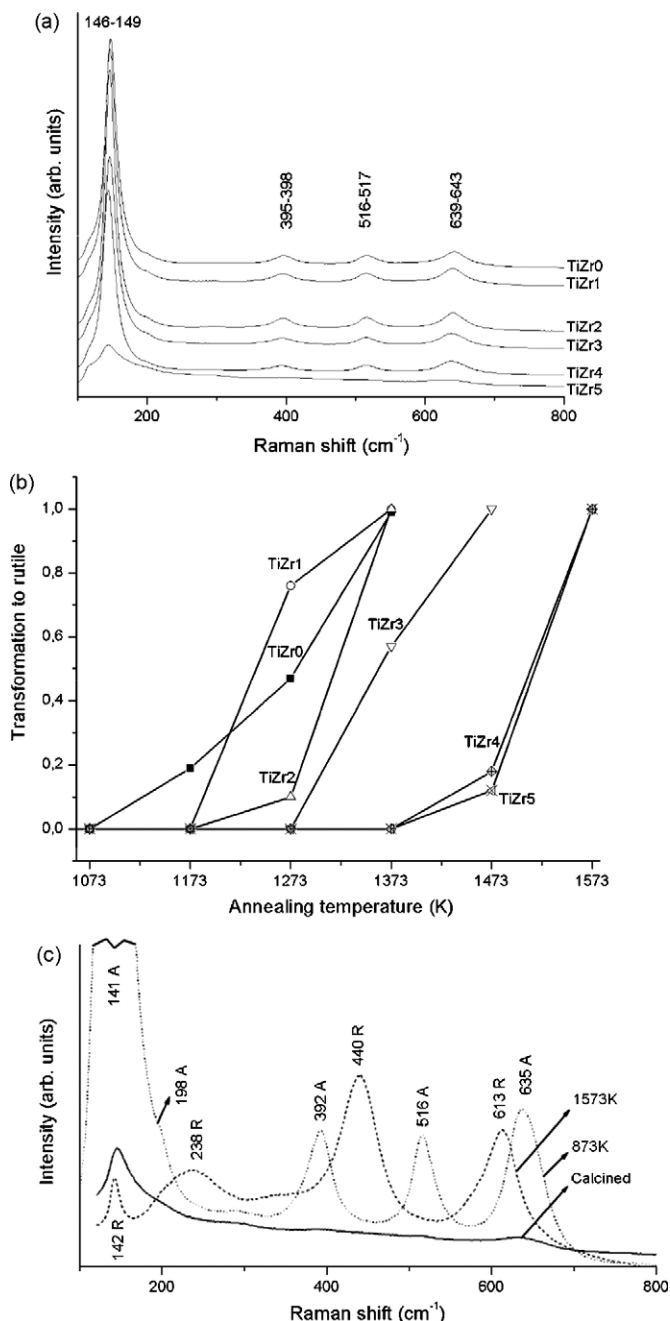


Fig. 3. (a) Raman spectra of Zr doped TiO₂. The spectra have been intensity shifted for clarity. Note the non-crystalline nature of the sample TiZr5. (b) Rutile content in the samples calculated from Eq. (1) plotted versus annealing temperature for each sample in the sample series TiZr0–5. The phase transition from anatase to rutile is retarded up to ~150 K by incorporating zirconium ions into the lattice. Note: A temperature gradient caused the readings to be overestimated by ~150 K for high annealing temperatures and less for lower annealing temperatures. (c) Evolution of Raman spectra of sample TiZr5 as a function of annealing temperature.

absorption bands in the 1100 cm⁻¹ region show that inorganic surface PO_x complexes form [34,35,41]. Several absorption bands due to differently coordinated PO_x species are expected to be present in this region, which are non-trivial to unambiguously identify [15,34,43]. The exact molecular vibrations depend on the charge of the P atom which in turn is affected by the surface coordination, hydrogen bonding and coupling to neighbouring adsorbates [15,35,41,43]. Furthermore, TiO₂ strongly absorb IR light below 1000 cm⁻¹ which prevents analysis of the metal-phosphorous peaks found below 1000 cm⁻¹ in DRIFT spectroscopy.

Photo-oxidation of the organic functional groups of DMMP (CH₃ and OCH₃) is expected to yield intermediate surface-coordinated aldehyde [35,44], formate [17,35,44,45,47,48], and carbonates species [35,44,49,50]. Moreover, these species can bind to the surface in several ways. For example, formate (HCOO), a stable organic oxidation product typically seen on TiO₂ following photo-oxidation of organics, can bind to the surface as a monodentate or bridging bidentate resulting in a distribution of possible $\nu(\text{CH})$, $\nu_a(\text{OCO})$, $\nu_s(\text{OCO})$ and $\nu(\text{CO})$ frequencies occurring between ca. 2800 and 2900, 1700–1540, 1400–1350 and 1100–1300 cm⁻¹, respectively [45,51,52]. In addition carbonate species (with varying degree of hydrogenation) have frequencies which occur in the same regions with similar coordination dependencies [16,35]. In Fig. 6 it is evident that formate and subsequently carbonate species are the dominant final surface products after extended UV illumination. The vibrational frequencies typically correspond to mixtures of ionic and adsorbed species suggesting high surface coverages and water formation on the surface. The latter is evidenced by the increased water bands between 3200 and 3500 cm⁻¹ (not shown in Fig. 6). In the C–H stretching region, vibrations due to DMMP are initially seen but with increasing UV irradiation time new peaks associated with formate appears at 2877 cm⁻¹, $\nu_a(\text{CH}_3)$, and the $\nu_s(\text{COO}) + \delta(\text{CH}_3)$ combination band at 2957 cm⁻¹. The final spectra in Fig. 6 obtained after 115 min illumination contain no (TiZr2) or small (TiZr0 and TiZr4) $\nu(\text{CH})$ bands and suggest that most of the DMMP is converted to inorganic species (carbonates and PO_x).

There are some notable differences clearly revealed by in situ DRIFT spectroscopy in Fig. 6 correlated to Zr doping. Comparing the different samples in the TiZr0–5 series the first obvious difference is the two large negative absorbance bands appearing with increasing illumination time at ca. 1432 and 1534 cm⁻¹ on the undoped TiO₂ sample (Fig. 6). As we have previously shown these bands are due to photodepletion of traces of urea residues from the sample synthesis that were not removed by the annealing at 673 K in synthetic air [12]. The absorbance band around 2204 cm⁻¹ which increases throughout the entire illumination time is due to isocyanato complexes (Ti–NCO), which are created from the photoreaction of urea residues [53]. The concentrations of isocyanato species become smaller with increasing Zr concentration (TiZr1, TiZr2 and to some extent also TiZr3) and they are completely absent for TiZr4 and TiZr5. This further corroborates the results that the concentration of urea residues is smaller on Zr doped TiO₂. This is in agreement with the reported shorter Ti–N bond lengths (and weaker bond strength) compared to corresponding Zr–N bonds in isocyanato complexes [54]. This further emphasizes that the reason for the low concentration of residual synthesis products on the highly Zr doped samples is likely to be found in the particle nucleation mechanism during synthesis. The 2204 cm⁻¹ absorbance band is correlated with large absorption bands at 1740 and 1685 cm⁻¹ and these are consequently attributed to aldehyde species and carbonyl bands in Ti–isocyanato complexes such as ureylene [55] formed during photoreactions with urea residues. As expected the 2204, 1740 and 1685 cm⁻¹ bands cannot be seen on the P25 reference sample. A closer examination of the spectra in Fig. 6 also reveals that there is a larger relative concentration of formate ions and μ -formate compared to other surface species on the Zr doped samples compared to undoped TiO₂ suggesting stronger formate bonding to Zr sites on Zr:TiO₂.

4.4. Photodegradation of CEES

Surface bonded sulphur oxide species (SO_x) form upon UV illumination of Zr:TiO₂ preadsorbed with CEES with typical absorption bands in the 1000–1200 cm⁻¹ region [56], Fig. 7. The

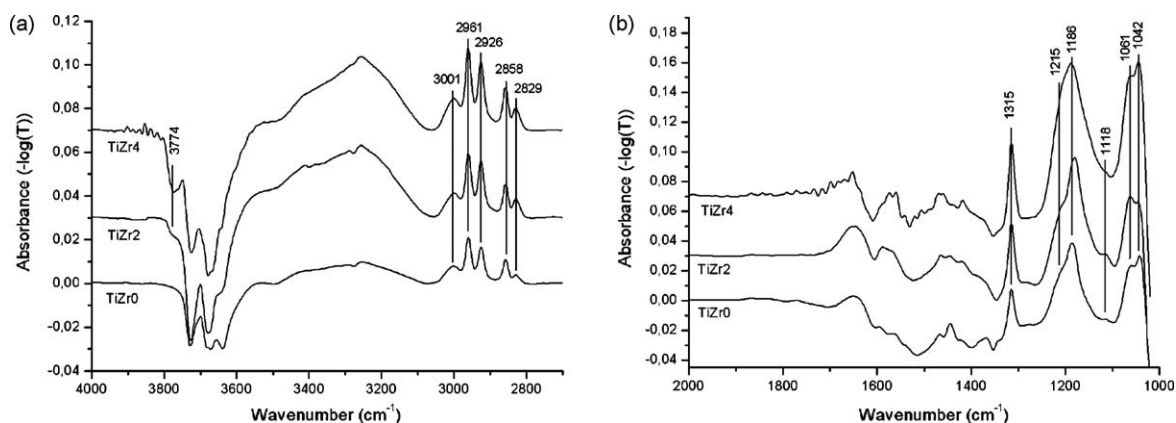


Fig. 4. (a and b) DRIFT spectra of DMMP adsorbed on TiZr0, TiZr2 and TiZr4.

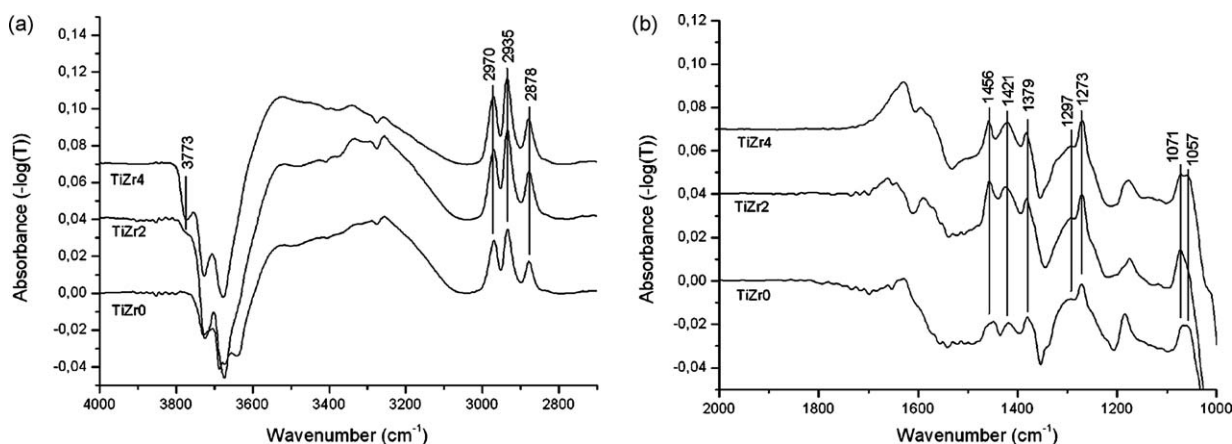


Fig. 5. (a and b) DRIFT spectra of CEES adsorbed on TiZr0, TiZr2 and TiZr4.

vibrational bands of these complexes include organic sulfoxide, sulphate and sulphonic acid complexes [35,40,41,56]. Photo-oxidation of the ethyl groups in CEES is expected to yield aldehydes, formate, acetates and carbonates. Even though qualitative assignments of the various intermediate surface species are possible based on the spectra shown in Fig. 7, an unambiguous quantification solely based on the DRIFT spectra is prohibited due to their overlapping absorbance together with the strong TiO_2 absorbance below 1000 cm^{-1} . Nevertheless typical spectral features from formate and (bi)carbonate intermediates can be identified. Compared to DMMP a relative higher concentration of adsorbed formate species may be evidenced by the peak at 1565 cm^{-1} upon CEES degradation, whose intensity decreases after long irradiation time (up and down arrows in Fig. 7). This is likely to be a consequence of the higher degradation rate of CEES relative DMMP which leads to accumulation of stable formate species on the surface. As for DMMP photo-oxidation, the concentration of formate species is much larger on the Zr doped samples compared to the pure TiO_2 samples (TiZr0 and P25). Again bands due to isocyanato complexes are only seen on the pure TiO_2 (TiZr0) and at the lowest Zr concentration (TiZr1).

4.5. Photodegradation rates of DMMP and CEES

Even though it is fairly straightforward to remove the urea residues present mainly on the undoped TiO_2 sample (TiZr0) [12] we have chosen not to incorporate further sample pre-treatments in the photoreaction studies presented here. The reason is four-fold: First, we have observed that upon Zr doping

further pre-treatments become unnecessary (Figs. 6 and 7). Second, by not introducing further sample pre-treatments it is possible to evaluate the as prepared samples on the same basis without modifying the structure (e.g. by annealing) or surface chemistry (e.g. by NaOH and acid cleaning) which may or may not be dependent on Zr dopant concentration. Third, inspired by the observation that Zr doping improves on the sample purity of the as prepared samples and that the intention here is to investigate a low cost photocatalyst manufacturing method makes further pre-treatment procedures somewhat miss the major target of the study. Finally, as described below we have used mode resolved IR bands of the parent molecules as well as the integrated absorbance band area in the C–H stretch region to distinguish between total organic decomposition rate (which contain urea residue contributions for TiZr0) and decomposition rates for the parent molecules. Our results show that the former yields a lower limit of the intrinsic parental molecule reaction rate [12].

For both DMMP and CEES similar mode resolved degradation rates, $k(\nu)$, were determined using a pseudo-first order rate law applied on the first 15 min of illumination. The corresponding UV illumination time needed to decrease the absorbance band area to 10% of their initial values, $t_{10}(\nu)$, were also determined as a practical measure of the materials effectiveness for DMMP and CEES removal, respectively. The $\nu(\text{CH}_3)$ band at 2926 cm^{-1} as well as the integrated $\nu(\text{C-H})$ absorbance between 3060 and 2700 cm^{-1} were used to determine $k(\nu)$ and $t_{10}(\nu)$ for DMMP (Fig. 8). These peaks are clearly resolved in all samples (in contrast to the absorption peaks of DMMP in the fingerprint region). By using the

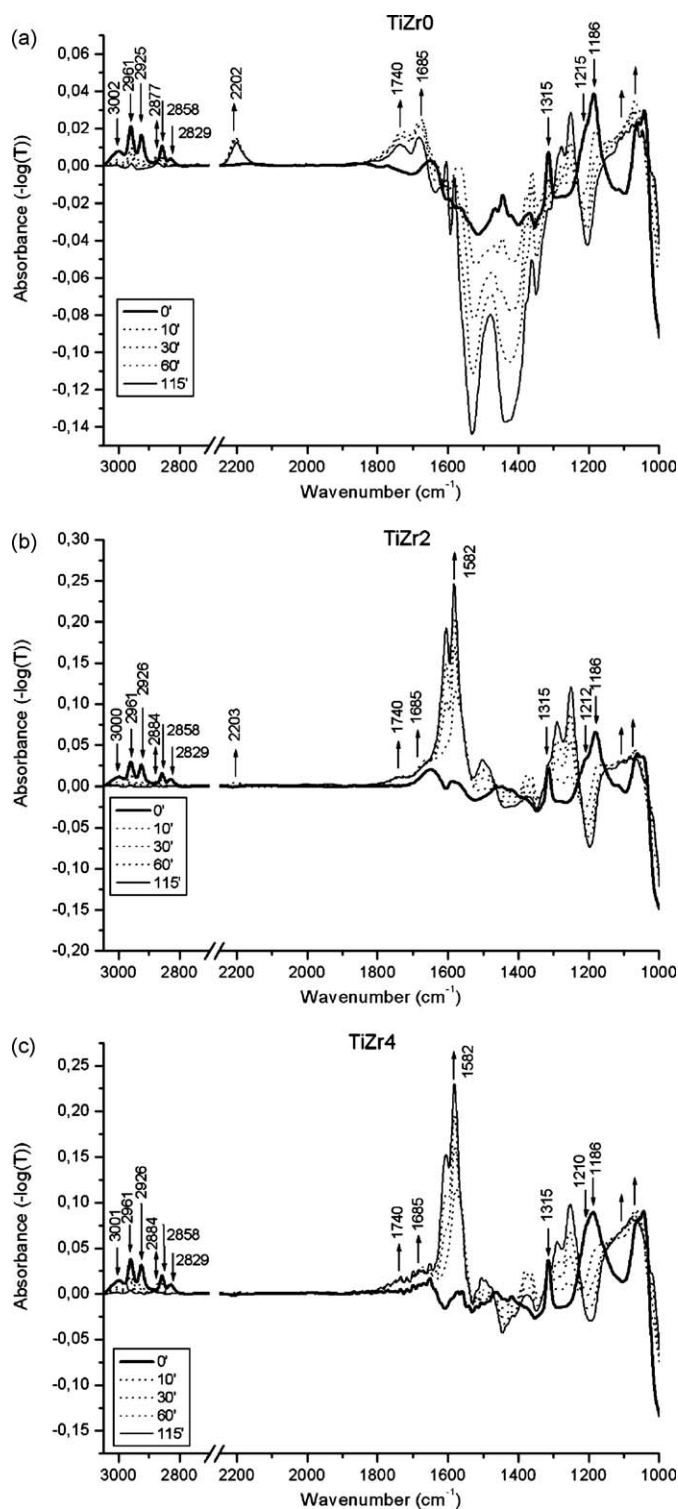


Fig. 6. In situ DRIFT spectra of DMMP adsorbed on (a) TiZr0, (b) TiZr2 and (c) TiZr4 at various times after UV irradiation.

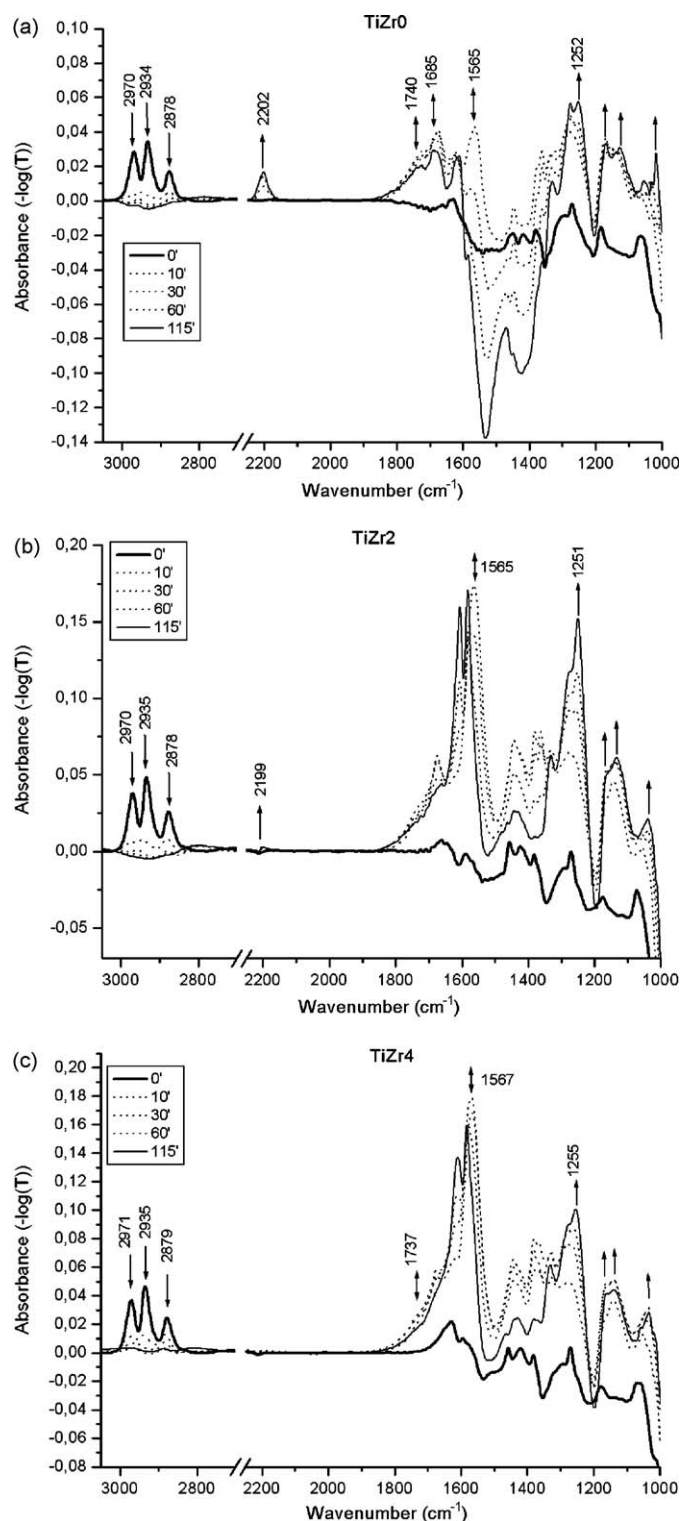


Fig. 7. In situ DRIFT spectra of CEES adsorbed on (a) TiZr0, (b) TiZr2 and (c) TiZr4 after various times after UV irradiation.

whole C–H region (3060–2700 cm⁻¹) an integrated rate constant is obtained, including any intermediate hydrocarbon species for the conversion of DMMP, which is the reason for the higher degradation rate for the $\nu(\text{CH}_3\text{P})$ band at 2926 cm⁻¹ compared to the integrated C–H absorbance band. The results show that the samples with low Zr content are more effective than the samples with high Zr concentration, and that the Zr samples TiZr1 and in particular TiZr2 exhibit a slightly higher degradation rate

compared to the P25 reference sample. The undoped TiO₂ sample (TiZr0) is equally efficient as the reference P25 sample.

The $\nu(\text{CH}_3)$ band at 2936 cm⁻¹ and the integrated $\nu(\text{C–H})$ absorbance between 3070 and 2670 cm⁻¹, were also used to determined $k(\nu)$ and $t_{10}(\nu)$ for CEES, Fig. 9. Again the results show that the TiO₂ samples with low Zr doping concentration are more efficient than those with high Zr concentration, and exhibit similar $k(\nu)$ as the undoped TiO₂ sample TiZr0. However in contrast to

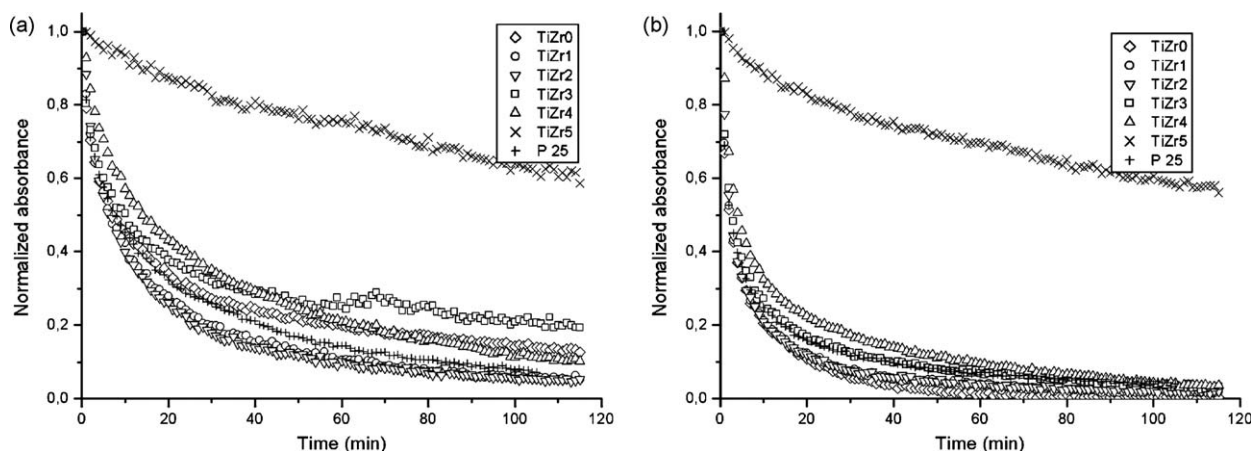


Fig. 8. The mode resolved absorbance vs. solar light illumination time for (a) the $\nu(\text{CH}_3)$ band and (b) the integrated C–H region in DMMP measured by in situ DRIFTS.

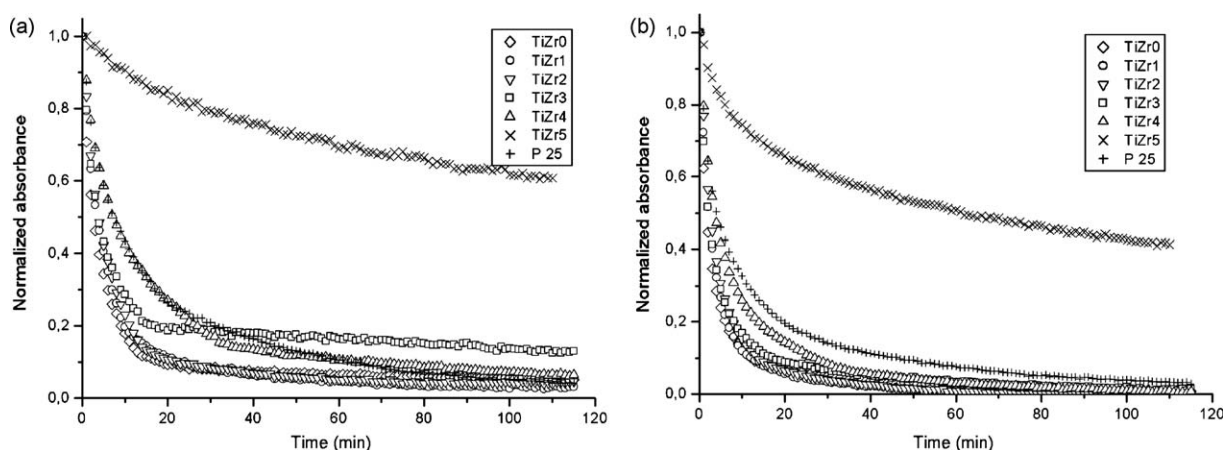


Fig. 9. The mode resolved absorbance vs. solar light illumination time for (a) the $\nu(\text{CH}_3)$ band and (b) the integrated C–H region in CEES measured by in situ DRIFTS.

DMMP photo-oxidation all samples in the TiZr0–TiZr4 have significantly higher $k(\nu)$ than P25. Again the samples with lowest Zr doping concentration exhibit the highest reactivity. Only the non-crystalline TiZr5 sample performs worse than P25.

5. Discussion

Our results show that small amounts of Zr doping of titania (1.5–6.8 wt% Zr) enhance the photocatalytic degradation rate. These results agree well with those reported by Venkatachalam et al. [5]. In this latter study an optimum of Zr^{4+} ion doping to TiO_2 was established to be about 3 mol% (~ 3.4 wt%) for photodegradation of 4-chlorophenol. In a related study employing an analogous synthesis method Štengl et al. [9] studied the photodegradation rate of Orange 2 dye in aqueous slurries containing Zr doped titania nanoparticles. They found that the decomposition rate increased with decreasing Zr doping concentrations and was highest on undoped titania. In all cases the decomposition rate was higher compared to P25. We note however that in both of the studies quoted above different experimental conditions (aqueous vs. gas phase) and UV illumination characteristics were employed, which prevents a direct comparisons of results. In the following we discuss the implications of our results further.

In the present study differences in surface area (Table 1) is effectively normalized by comparing the removal of adsorbates on a saturated surface at different times after irradiation using DRIFT

spectroscopy, i.e. the change in coverage rather than number of absorbents is measured. Indeed by inspection of our results we cannot correlate the photodegradation rate in Table 1 with the specific surface area. Neither is the reported UV–vis absorbance very different for $\text{Zr}:\text{TiO}_2$. In fact, we and others have previously reported a slight blue-shift upon low Zr doping of titania [5,57]. XRD and Raman data both show an incorporation of Zr in the anatase lattice, and Raman experiments also reveal that Zr stabilizes the anatase structure. Making the anatase structure more durable is beneficial in applications where sintering and possibly phase transformation are problems; rutile is known to be a poorer photocatalyst [57,58]. However the presence of a Zr–OH vibration mode at 3773 cm^{-1} observed in DRIFT spectroscopy show that Zr is present on the surface. This proves that Zr modifies the surface chemistry, which in turn has implications for hole attachment to surface OH groups and adsorbate bonding. In fact it has been pointed out that an increased reactivity due to addition of Zr may be a consequence of higher surface acidity of surface Zr–OH groups [6,36]. In another study Yu et al. [59] proposed a mechanism involving lattice O^{2-} and O^- species adsorbed on $\text{Zr}:\text{TiO}_2$, which was modulated by Zr doping to explain a maximum reactivity occurring at 7.5 wt%. This is in qualitative agreement with a recent study of Zr doped TiO_2 by Mattsson et al. [18] where an increased diffusion of photoexcited O atoms was inferred upon Zr doping. A possible explanation of an optimum photoreactivity at intermediate Zr doping concentration may be found in the spectra

shown in Figs. 6 and 7. There it was inferred that the relative concentration of adsorbed formate and carbonate species was higher on Zr:TiO₂ (Sections 4.3 and 4.4). Thus it may be speculated that at intermediate Zr concentrations there is a balance between increased hole attachment rate, surface diffusivity and strong bonding of surface intermediates (primarily formate and carbonate complexes). The exact mechanism(s) responsible for the beneficial photoreactivity remains however to be proven.

6. Conclusions

The structure and photocatalytic activity of Zr doped TiO₂ nanocrystallites with a varying Zr content between 0 and 15 wt% prepared by a cost-effective, efficient and environmentally benign method has been measured by vibrational spectroscopy and XRD. It is shown that the presence of Zr⁴⁺ ions delays the phase transformation to rutile upon annealing as well as retarding grain coarsening. Both properties are expected to be beneficial for sustained photoreactivity. Particles with anatase structure forms by annealing amorphous phase Zr:TiO₂ with Zr in excess of 10 wt%.

All samples except the non-crystalline TiZr5 exhibit significant photoactivity for decomposition of CEES and DMMP in synthetic air at room temperature. Intermediate decomposition products such as sulphur complexes, phosphor complexes, carboxylates, aldehydes, acetates, and carbonate complexes can be identified on the samples after UV irradiation. They are all expected surface intermediates that have been previously reported in the literature. Photodecomposition of intermediate hydrocarbon species occur during the whole 60 min measurement period on all samples except TiZr5 (the amorphous sample). On the undoped TiO₂ sample urea residues are detected spectroscopically. Much less is detected on the Zr doped samples. Photoreactions with urea residues results in the formation of stable isocyanato complexes on the surface. Mode resolved FTIR surface spectroscopy enables distinction of CEES or DMMP and urea residue surface chemistry and intra-comparable reaction rates can be obtained. The most efficient sample for photodegradation of CEES and DMMP is shown to be TiZr2 with a fairly low Zr concentration (6.8 wt%). The photodegradation rate of CEES is higher on all samples in the TiZr series (except TiZr5) compared to P25. For DMMP the TiZr0, TiZr1 and TiZr2 show degradation rates similar or higher than P25. The photodegradation of CEES is faster than DMMP under the same experimental conditions.

References

- [1] A. Fujishima, X. Zhang, D.A. Tryk, *Surf. Sci. Rep.* 63 (2008) 515.
- [2] M.R. Hoffmann, S.T. Martin, W. Choi, D.W. Bahnemann, *Chem. Rev.* 95 (1995) 69.
- [3] D.F. Ollis, H. Al-Ekabi, *Photocatalytic Purification and Treatment of Water and Air*, Elsevier, Amsterdam, 1993.
- [4] J.T. Chen, J. Wang, F. Zhang, G.A. Zhang, Z.G. Wu, P.X. Yan, *J. Crystal Growth* 310 (2008) 2627.
- [5] N. Venkatachalam, M. Palanichamy, B. Arabindoo, V. Murugesan, *J. Mol. Catal. A* 266 (2007) 158.
- [6] M. Hernández-Alonso, J.M. Coronado, B. Bachiller-Baeza, M. Fernández-García, *J. Soria, Chem. Mater.* 19 (2007) 4283.
- [7] M.E. Manríquez, T. López, R. Gómez, J. Navarrete, *J. Mol. Catal. A* 220 (2004) 229.
- [8] J. Lukáč, M. Klementová, P. Bezdicka, S. Bakardjieva, J. Šubrt, L. Szatmáry, A. Grusková, *J. Mater. Sci.* 42 (2007) 9421.
- [9] V. Štengl, S. Bakardjieva, N. Murafa, F. Opluštil, *Open Process Chem. J.* 1 (2008) 1.
- [10] JCPDS PDF-2 Database, International Centre for Diffraction Data database, 2001, www.icdd.com.
- [11] B.D. Cullity, *Elements of X-Ray Diffraction*, Addison-Wesley, Reading, MA, 1978.
- [12] L. Österlund, S. Štengl, A. Mattsson, S. Bakardjieva, P.O. Andersson, F. Opluštil, *Appl. Catal. B* 88 (2009) 194.
- [13] J.-G. Li, T. Ishigaki, *Acta Mater.* 52 (2004) 5143.
- [14] A.L. Bassi, D. Cattaneo, V. Russo, C.E. Bottani, E. Barborini, T. Mazza, P. Piseri, P. Milani, F.O. Ernst, K. Wegner, S.E. Pratsinis, *J. Appl. Phys.* 98 (2005) 074305.
- [15] A. Kiselev, M. Andersson, A. Palmqvist, L. Österlund, *J. Photochem. Photobiol. A: Chem.* 184 (2006) 125.
- [16] T. van der Meulen, A. Mattsson, L. Österlund, *J. Catal.* 251 (2007) 131.
- [17] M. Andersson, A. Kiselev, L. Österlund, A.E.C. Palmqvist, *J. Phys. Chem. C* 111 (2007) 6789.
- [18] A. Mattsson, M. Leideborg, L. Persson, G. Westin, L. Österlund, *J. Phys. Chem. C* 113 (2009) 810.
- [19] A. Mattsson, M. Leideborg, K. Larsson, G. Westin, L. Österlund, *J. Phys. Chem.* 110 (2006) 1210.
- [20] J.L. Shi, J.H. Gao, *J. Mater. Sci.* 30 (1995) 793.
- [21] T. Ohsaka, F. Izumi, Y. Fujiki, *J. Raman Spectrosc.* 7 (1978) 321.
- [22] H. Richter, Z.P. Wang, L. Ley, *Solid State Commun.* 39 (1981) 625.
- [23] M. Saif, M.S.A. Abdel-Mottaleb, *Inorg. Chim. Acta* 360 (2007) 2863.
- [24] M. Hirano, K. Ota, T. Ito, *J. Am. Ceram. Soc.* 88 (2005) 3303.
- [25] Y. Wan, J. Ma, W. Zhou, Y. Zhu, X. Song, H. Li, *Appl. Catal. A* 277 (2004) 55.
- [26] D.J. Reidy, J.D. Holmes, M.A. Morris, *J. Euro. Ceram. Soc.* 26 (2006) 1527.
- [27] S. Kelly, F.H. Pollak, M. Tomkiewicz, *J. Phys. Chem.* 101 (1997) 2730–2734.
- [28] M. Hirano, C. Nakahara, K. Ota, O. Tanaike, M. Inagaki, *J. Solid State Chem.* 170 (2003) 39–47.
- [29] S.P.S. Porto, P.A. Fleury, T.C. Damen, *Phys. Rev.* 154 (1967) 522.
- [30] H. Zhang, B. J.F., *J. Mater. Chem.* 8 (1998) 2073.
- [31] T. Mazza, E. Barborini, P. Piseri, P. Milani, *Phys. Rev. B* 75 (2007) 045416.
- [32] L. Bertilsson, E.I.B. Liedberg, *J. Phys. Chem.* 101 (1997) 6021.
- [33] D.A. Trubitsyn, A.V. Vorontsov, *J. Phys. Chem.* 109 (2005) 21884.
- [34] C. Rusu, J.T. Yates Jr., *J. Phys. Chem.* 104 (2000) 12292.
- [35] K. Nakamoto, *Infrared and Raman Spectra of Inorganic and Coordination Compounds*, 5th ed., John Wiley & Sons, New York, 1997.
- [36] X. Fu, L.A. Clark, Q. Yang, M.A. Anderson, *Environ. Sci. Technol.* 30 (1996) 647.
- [37] T.L. Thompson, D.A. Panayotov, J.T. Yates Jr., *J. Phys. Chem.* 108 (2004) 16825.
- [38] *The Aldrich Library of FT-IR Spectra*, Second Edition, Aldrich, Milwaukee, 1997.
- [39] D.B. Mawhinney, J.A. Rossin, K. Gerhart, J.T. Yates Jr., *Langmuir* 15 (1999) 4789–4795.
- [40] A.V. Vorontsov, C. Lion, E.N. Savinov, P.G. Smirniotis, *J. Catal.* 220 (2003) 414.
- [41] G. Socrates, *Infrared and Raman Characteristic Group Frequencies*, 3rd ed., John Wiley & Sons, Chichester, 2001.
- [42] P.A. Connor, A.J. McQuillan, *Langmuir* 15 (1999) 2916.
- [43] J.M. Coronado, S. Kataoka, I. Tejedor-Tejedor, M.A. Anderson, *J. Catal.* 219 (2003) 219.
- [44] L. Österlund, A. Mattsson, in: L. Vayssieres (Ed.), *Solar Hydrogen and Nanotechnology*, vol. 6340, SPIE, Bellingham, 2006.
- [45] L.-F. Liao, W.-C. Wu, C.-Y. Chen, J.-L. Lin, *J. Phys. Chem.* 105 (2001) 7678.
- [46] B.E. Hayden, A. King, M.A. Newton, *J. Phys. Chem.* 103 (1999) 203.
- [47] G.B. Deacon, R.J. Phillips, *Coord. Chem. Rev.* 33 (1980) 227.
- [48] A.A. Davydov, *Infrared Spectroscopy of Adsorbed Species on the Surface of Transition Metal Oxides*, John Wiley & Sons, New York, 1990.
- [49] F.P. Rotzinger, J.M. Kesselman-Truttman, S.J. Hug, V. Shklover, M. Grätzel, *J. Phys. Chem.* 108 (2004) 5004.
- [50] J.R.S. Brownson, I.M. Tejedor-Tejedor, M.A. Anderson, *Chem. Mater.* 17 (2005) 6304–6310.
- [51] P. Hauck, A. Jentys, J.A. Lercher, *Appl. Catal. B* 70 (2007) 91.
- [52] S.J. Anderson, D.S. Brown, K.J. Finney, *J. Chem. Soc., Dalton Trans.* (1979) 152.
- [53] M. García-Hernández, U. Birkenheuer, A. Hu, F. Illas, N. Röscher, *Surf. Sci.* 471 (2001) 151.
- [54] S. Kataoka, E. Lee, I. Tejedor-Tejedor, M.A. Henderson, *Appl. Catal. B* 61 (2005) 159.
- [55] L. Österlund, A. Mattsson, M. Leideborg, G. Westin, in: S. Mathur, M. Singh (Eds.), *Nanostructured Materials and Nanotechnology: Ceramic Engineering and Science Proceedings*, vol. 28, John Wiley & Sons, 2007.
- [56] K. Tanaka, M.F.V. Capule, T. Hisanaga, *Chem. Phys. Lett.* 187 (1991) 73.
- [57] J.C. Yu, J. Lin, R.W.M. Kwok, *J. Phys. Chem.* 102 (1998) 5094.